Label-Free Raman Spectral Imaging of Intracellular Delivery and Degradation of Polymeric Nanoparticle Systems

Tatyana Chernenko,[†,][*] Christian Matthäus,[†] Lara Milane,[‡] Luis Quintero,[§] Mansoor Amiji,[‡,][*] and Max Diem[§,][*]

[†]Department of Chemistry and Chemical Biology, Northeastern University, Boston, Massachusetts 02115, [‡]Department of Pharmaceutical Sciences, School of Pharmacy, Northeastern University, Boston, Massachusetts 02115, and [§]College of Engineering, University of Puerto Rico, Mayagües, Puerto Rico 00680

ABSTRACT Novel optical imaging methods, such as Raman microspectroscopy, have been gaining recognition in their ability to obtain noninvasively the distribution of biochemical components of a sample. Raman spectroscopy in combination with optical microscopy provides a label-free method to assess and image cellular processes, without the use of extrinsic fluorescent dyes. The submicrometer resolution of the confocal Raman instrumentation allows us to image cellular organelles on the scale of conventional microscopy. We used the technique to monitor subcellular degradation patterns of two biodegradable nanocarrier systems—poly-(ε-*caprolactone*) (PCL) and poly(lactic-*co*-glycolic acid) (PLGA). Our results suggest that both drug-delivery systems eventually are incorporated into Golgi-associated vesicles of late endosomes. These processes were monitored *via* the decrease of the molecule-characteristic peaks of PCL and PLGA. As the catabolic pathways proceed, shifts and variations in peak intensities and intensity ratios in the rendered Raman spectra unequivocally delineate their degradation patterns.

N anoparticulate drug carriers are useful for achieving target-specific delivery of chemotherapeutics and for enhancing the intracellular availability of a therapeutic payload. The use of drug carriers can transform exogenous molecules with undesirable pharmacokinetics into therapeutic agents. Immunotherapeutic as well as chemotherapeutic strategies may also benefit from nanodelivery systems due to their potential in vaccine administration. Research in this area is focused on finding mucous-penetrating nanoparticles, which may be nasally administered, thus decreasing the need for injections and potentially even allowing self-treatment.[1,2] Gene therapy has also recruited the use of nanodelivery systems due to its potentially beneficial application in treatments of genetic disorders, chronic diseases, as well as chemotherapy.

Materials utilized for the preparation of various drug-delivery systems range from polymers—such as biodegradable polyesters[3−9]—to inorganic material, as

for example gold, silicon, or iron oxide nanoparticles.[10] The most extensively utilized nanoparticles for *in vivo* use are micelles, liposomes, and diverse polymeric nanostructures.[7,11] This is due to the ease of drug and contrast-agent encapsulation as well as their biocompatibility within the body.

With all the promising applications, there are a number of concerns with the materials available for fabrication of diverse nanocarriers, such as their ability and degree of intracellular penetration, organelle specificity, drug release patterns, as well as their ultimate degradation kinetics. Even though numerous experiments have been performed determining the retention of nanoparticles and their encapsulated drugs within the body, subsequent cytotoxicity in the targeted tissue, and the possible side effects in surrounding healthy tissue,[12−17] little is known on the fate, consequences, and impact of the nanoparticles on intracellular homeostasis.[14,18] It is thus critical to parallel the development of diverse nanodevices with improved methods establishing their biocompatibility, intracellular trafficking, and dynamics.

The most common technique for studying the intracellular behavior of nanocarriers is to encapsulate a fluorophore or a fluorophore-labeled drug derivative and subsequently image the system using fluorescence microscopy. The information provided from this analysis, however, is limited due to the potential of the fluorophore to leak out of the system and the extent of its interference with the biochemical behavior of the labeled molecule. Furthermore, this method does not provide information regarding nanocarrier/payload association and dissociation patterns, which is the ultimate purpose for the carrier system and a

crucial issue in nanotechnology. Low contrast, autofluorescence, and photobleaching also confound fluorescent microscopy, compromising the continuous monitoring of the same sample.

Raman spectroscopy in combination with optical microscopy provides a novel noninvasive and a label-free method to assess and image cellular processes based on their biochemical changes.[19−21] The technique is based on the identification of molecular vibrations that are characteristic of distinct functional groups that comprise molecules. For cells and tissues, these vibrational fingerprints arise from the functional groups of proteins, nucleic acids, lipids, phospholipids, and carbohydrates—which framework the basic building blocks of mammalian cells. Vibrational spectra may be obtained by illuminating the specimen either with infrared radiation or laser light in the visible range of the spectrum. The latter approach is based upon the inelastic scattering of photons and is known as the Raman effect.

Raman microspectroscopy technique affords minimal sample preparation, high sensitivity to small intracellular fluctuations, as well as high spatial resolution. Raman spectra from within the cell reflect the biochemical composition found within the laser focal volume of approximately $0.3 \times 0.3 \times 1.3 \ \mu m^3$ in size, which is determined by the diffraction limit of the applied laser light.[22,23] Using the spectral parameters of a cell's components, it is possible to image cellular organelles such as the nucleus, chromatin, mitochondria, and lipid bodies, without the use of external labels or dyes at the resolution of conventional microscopy.[22,24−29]

Cellular spectra thus recorded display a large number of vibrations across a broad spectral range (500−4000 cm^{-1}), which are a superposition of bands that are descriptive of the functional groups of diverse molecules. The most dominating peaks in the Raman spectrum are due to the C−H stretching vibrations and are seen between 2800 and 3020 cm^{-1}. Carbonyl stretching modes of the peptide moiety (often referred to as amide I band) are located around 1650 cm^{-1}, C−H bending deformations at 1450 cm^{-1}, and coupled C_α−H/N−H bends of the peptide linkages between 1200 and 1400 cm^{-1} (also called amide III band).[30] Carbonyl stretches of ester residues appear around 1730−1760 cm^{-1}, depending on the overall molecular structure, which determines the position of the band. Spectral differences of cellular components have been previously addressed and are therefore not discussed in detail.[22,25,27,31]

RESULTS AND DISCUSSION

We have studied two nanocarrier systems of biodegradable and biocompatible polymers—poly(ε-caprolactone) (PCL) and poly(lactic-*co*-glycolic acid) (PLGA). Both systems are modified with poly(ethylene oxide) (PEO) chains to enhance circulation time and prevent
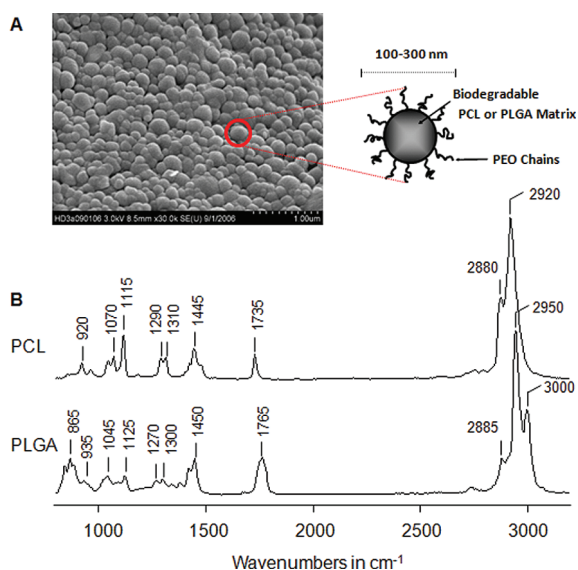

Figure 1. (A) SEM image of PCL nanoparticles. The schematic on the right illustrates the basic content of the 100−300 nm particle, which contains either PCL or PLGA biodegradable matrix with PEO chains extending outside. (B) Raman spectra of the PCL and the PLGA nanoparticles, demonstrating their characteristic peaks at 1730 and 2920 cm^{-1} for PCL and 1760 and 2950 cm^{-1} for PLGA.

aggregation. The reasons for widespread utilization of these polyester materials include their slow degradation *in vivo*,[32] increased tumor accumulation, and longer intratumoral retention due to the enhanced permeability and retention (EPR) effect.[33] *In vitro* studies have been performed on both systems to test their biocompatibility, toxicity effects, and stability,[32] having their degradation kinetics characterized using a dialysis membrane/buffer/aqueous media system with or without the presence of lipase.[4,32,34,35]

Thus, we have analyzed pure nanoparticles in order to establish a biochemical signature of their intracellular degradation pathway using a label-free method of detection as well as the behavior of the carrier platform without the drug load. The Raman spectral signatures of the raw components are shown in Figure 1. PCL and PLGA both exhibit their highest peak intensities in the C−H stretching regions at 2920 and 2950 cm^{-1}, respectively. The C=O stretches specific to the ester linkages are located at 1735 and 1765 cm^{-1}. Other Raman peaks of less intensity can be observed between 1000 and 1500 cm^{-1}.

In the experiments performed, we have incubated HeLa cells in medium containing a nanoparticle system at a concentration of 0.2 mg of nanoparticles per 1 mL of media for different time intervals. After incubation with the nanoparticles, the medium was removed and cells were either fixed immediately or continued to be grown with fresh medium in order to follow subsequent digestion patterns.

Since cellular spectra are the superposition of all cellular components, most of the nanoparticle-characteristic peaks tend to overlap with diverse subcellu-

lar biochemical signatures. Hence, Raman hyperspectral data sets obtained were analyzed using a mathematical algorithm known as Vertex Component Analysis (VCA), which decomposes complex spectra into its component (endmember) spectra[36,37] and presents distribution images of these endmembers. These abundance plots are scaled and converted to monochrome displays, where high color intensity denotes large endmember contributions. Three such endmember abundance plots are converted to RGB format and overlaid to give pseudocolor images of the cells. In the following images, blue regions represent cell body proteins, red regions represent the spectral patterns of the nanoparticles, green regions the lipid or phospholipid content of membrane-rich organelles such as the mitochondria, ER and Golgi, while structures likely to be endosomal vesicle formations are shown in yellow.

An incubation time for pure PCL nanoparticles of 7 h was chosen as a starting point based on the reproducibility of the uptake experiments. After 7 h, all imaged cells showed observable PCL inclusions. Shorter incubation times led to nanoparticle aggregations in fewer cells. Longer incubation times, on the other hand, did not result in an increased intracellular nanoparticle concentration. It is thus reasonable to assume that after 7 h a certain level of saturation is reached of nanoparticle penetration and their intracellular accumulation, undoubtedly, a cell-type-specific characteristic. It has been previously demonstrated that uptake efficiency shows linear dependencies at low concentrations and reaches a plateau at high dosages, underscoring a saturation behavior.[38] Thus, nanoparticle degradation patterns were followed after nanoparticle-containing medium was replaced at 7 h with fresh medium. This allows intracellular metabolic pathways to proceed without continuous nanoparticle integration.

After incubation of cells with PCL-containing medium for 7 h, intracellular inclusions became distinguishable in the cell body (Figures 2 and 3, top row). Since HeLa cells do not exhibit inherent intracellular phospholipid inclusions or lipid droplets, their formation is a direct consequence of incubation of the cell culture with the nanoparticle-containing medium. Figure 2 shows a Raman image of a HeLa cell incubated with the PCL particles for 7 h, constructed *via* the VCA algorithm, along with the corresponding endmember spectra. Spectrum A (red) exhibits the main spectral features as the Raman spectrum of pure PCL particles. The peak position of the C—H stretching band between 2800 and 3020 cm^{-1} is still centered at 2920 cm^{-1}, and the band shape appears almost unaltered compared to the reference spectrum shown in Figure 1. The characteristic peak of the C$\equiv$O stretching of the carboxyl ester at 1735 cm^{-1} is still found at the same position. Furthermore, the Raman bands at 920, 1115, 1290, and 1310 cm^{-1} are still observed. The spectrum is superimposed
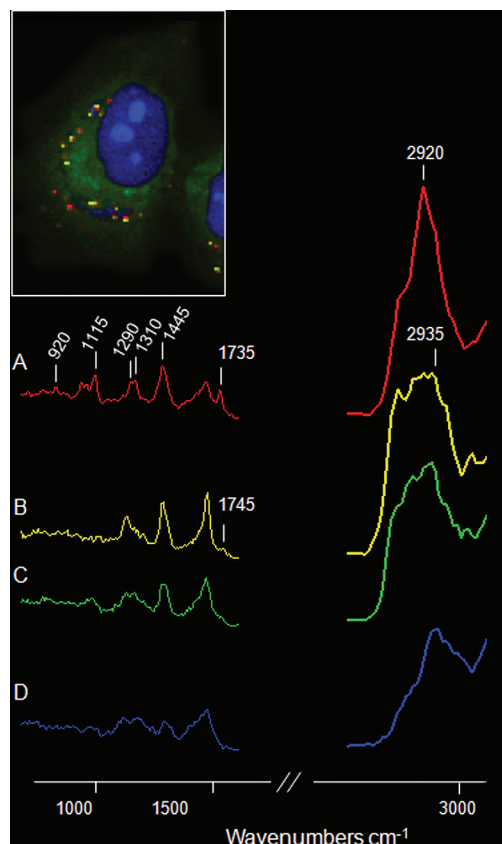

Figure 2. Inset: Pseudocolor Raman image (VCA analysis) of a HeLa cell incubated with PCL-particle-containing medium for 7 h. Red regions, PCL aggregates; yellow regions, lipid/phospholipid inclusions; green regions, membrane-rich organelles such as ER, Golgi, mitochondria; blue regions, proteins of the cell body. Traces A−D represent the Raman spectra of the corresponding regions.

on additional cellular features (*e.g.*, the amide I band at 1650 cm^{-1}), which is associated with protein vibrations. The largest abundance of the features corresponding to spectrum 2A is shown as intracellular red dots in Figure 2, where the nanoparticle aggregates appear to be randomly distributed throughout the cytoplasm. The spectral features observed for the yellow regions can be identified as subcellular structures or organelles that are rich in lipids or phospholipids because the Raman spectra of isolated lipids or phospholipids are almost identical.[39,40] These lipid-rich inclusions appear along with the nanoparticle aggregations and in some cases overlap them, as seen by the yellow features in Figure 2. The corresponding spectrum has a fingerprint prevalent in the diverse subcellular vesicle formations, exhibiting phospholipid-characteristic peaks in the C—H stretching region, as well as the peak at 1745 cm^{-1}, corresponding to the ester linkages. The existence of these inclusions can be explained by the formation of endocytotic vesicles in the cell upon engulfment of the nanoparticles.[18,41,42] The co-localization of nanoparticles and vesicles of high lipid content was ob-

served for all cells incubated for 7 h. Further examples are shown in Figure 3.

Incubation of the cells with fresh medium after 7 h incubation with PEO-PCL-containing medium terminates the incorporation of any new exogenous material. This allows mapping of the intracellular degradation patterns of the nanoparticles (Figure 3, middle row). It is evident from the VCA abundance plots that PCL particles do not get fully degraded even after 24 h, with the amount of digestion varying from cell to cell. As the internal translocation and sorting of the nanoparticles persists, their spectral features merge with the spectral characteristics of the cellular components. For example, the 1735 cm^{-1} signal is replaced by a shallower and broader peak at 1745 cm^{-1}. In addition, the peak at 2920 cm^{-1} decreases and is accompanied by an increase of several additional peaks in the C—H stretching region (spectra not shown). This can be explained by an increasing density of phospholipids encompassing the nanoparticles, detected *via* an increase in the aliphatic side chain vibrational bands. Such integration of the nanocarriers into vesicles of high phospholipid content, or secondary endosomes, is consistent with previous studies, where early and secondary endosome formation was detected with nanoparticle internalization,[18,38] as part of their metabolic pathway.

When the incubation time is increased from 7 to 17 h in fresh medium, the signatures of the PCL components are less pronounced and are masked by the signatures coming mostly from the intracellular vesicles (Figure 3, bottom row). Some of these vesicles accumulating the nanoparticles are associated with the Golgi complex.[18] This can be further seen from the yellow and light green inclusions in the green regions of the cell body, which depict membrane-rich organelles such as the endoplasmic reticulum and Golgi apparatus. The nanoparticles, however, do not seem to be associated specifically with either of the organelles, but rather seem to be enwrapped in Golgi-associated vesicles of the late endosomes. Thus, longer incubation of the cell culture with the fresh medium reveals a decrease in PCL-specific peaks. However, the phospholipid inclusions still remained prevalent, seen in the middle and bottom rows of Figure 3. This is due to the slow degradation of the PCL particles, where the engulfed nanoparticles, *via* secondary endosome formation, fuse with lysosomes for further degradation.[18,38,43]

Diverse metabolic pathways may thus be followed *via* spectral changes. First, the degradation of the nanoparticles occurs *via* hydrolysis of the ester bonds, which is observed as the decrease/disappearance of the 1735 cm^{-1} peak. Furthermore, subcellular sorting of the nanocarriers can be monitored by the variations of the C—H stretching region, which changes from one prominent peak at 2920 cm^{-1} to a broader and more jagged peak due to engulfment of the nanoparticles and sub-
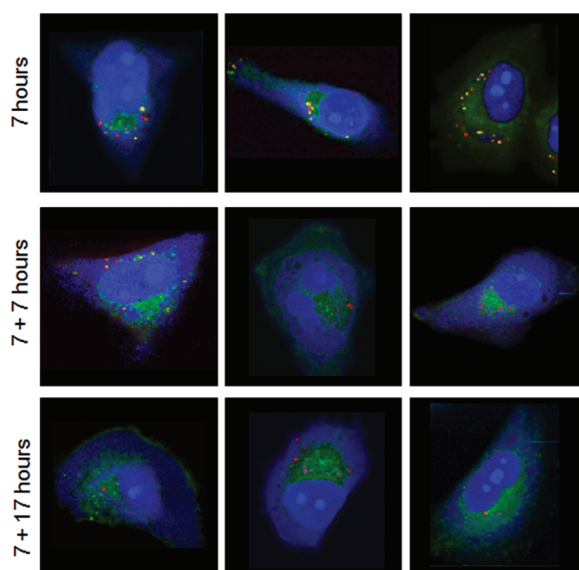

Figure 3. Time course of PCL nanoparticle degradation patterns obtained from Raman imaging/VCA analysis. Red regions represent PCL aggregates, green regions high lipid/phospholipid content, and blue regions the proteins of the cell body. Top row: images of cells after 7 h incubation with PCL-containing medium. Middle row: images of cells incubated with PCL-containing medium for 7 h followed by incubation with fresh medium for another 7 h. Bottom row: images of cells incubated in PCL-containing medium for 7 h followed by incubation for another 17 h in fresh medium.

sequent integration of the PCL signal with that of the intracellular vesicle formations.

Along with offering insight into the characteristic intracellular behavior of the nanoparticles, Raman imaging is able to provide insight into their penetration behaviors. At all time points sampled, the nanoparticles seem to aggregate after the cellular entry. The nanoparticles themselves are about 200 nm in size. With a spatial resolution of *ca.* 300 nm, we are most likely not able to observe individual nanoparticles. The intracellular inclusions observed, however, were consistently on the order of 1—2 μm in size, underscoring their aggregation. This result parallels data obtained on *in vivo* imaging of quantum dots' aggregation in tumor vasculature.[14,44]

Thus, cellular vibrational signatures are able to describe the subcellular pathway of the distribution of PCL nanoparticles *via* decreases, increases, and shifting of molecule-characteristic peaks. Following these variations can further portray the fate of the PCL particles, their metabolism, and excretion. We can follow the uptake and the distribution of PCL nanoparticles *via* their chemical signatures within the cell, noninvasively mapping the distribution and degradation patterns.

Another biocompatible material in extensive use as a biodegradable polymer is PLGA, which has been shown to have faster kinetics then PCL.[6,32] We have incubated HeLa cells with the PLGA-nanoparticle containing medium for 2 h, after which they were fixed and imaged (Figure 4). The signatures from the endocytosed
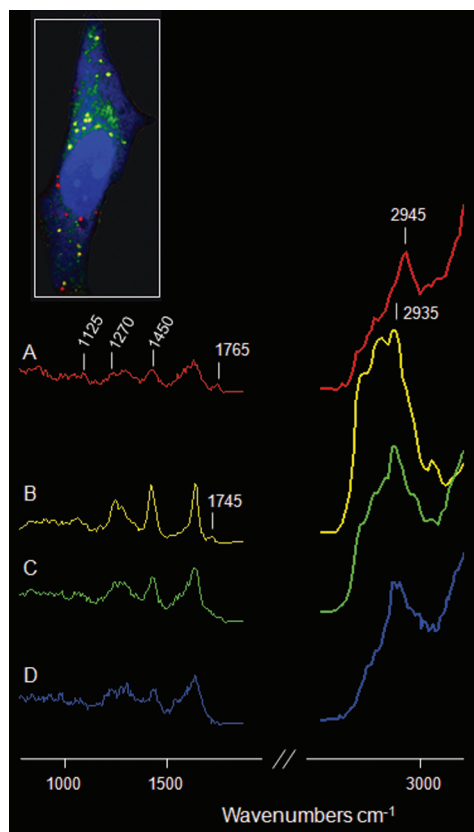
Figure 4. Inset: Pseudocolor Raman image (VCA analysis) of a HeLa cell incubated with PLGA-containing medium for 2 h. Red regions, PLGA aggregates; yellow regions, denote lipid/phospholipid inclusions; green regions, membrane-rich organelles such as ER, Golgi, mitochondria; blue regions, proteins of cell body. Traces A–D represent the Raman spectra of the corresponding regions.
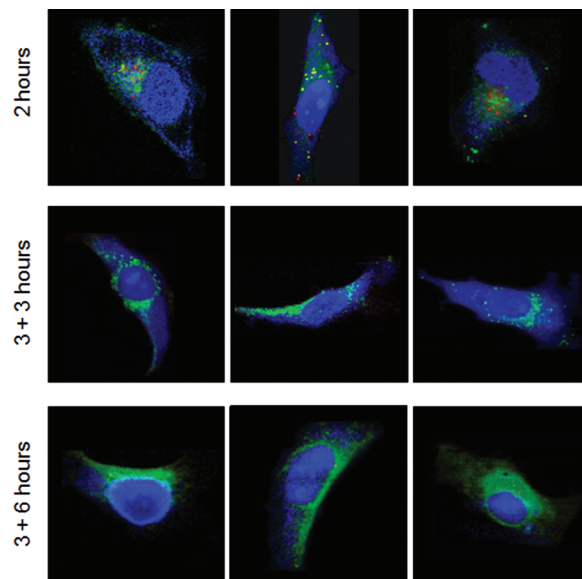

Figure 5. Time course of PLGA nanoparticle degradation patterns obtained from Raman imaging/VCA analysis. Red regions represent PLGA aggregates, green regions high lipid/phospholipid content, and blue regions the proteins of the cell body. Top row: images of cells after 2 h incubation with PLGA-containing medium. Middle row: images of cells incubated with PLGA-containing medium for 3 h followed by incubation with fresh medium for another 3 h. Bottom row: images of cells incubated in PLGA-containing medium for 3 h followed by incubation for another 6 h in fresh medium.

PLGA nanoparticles may be followed by the characteristic peak intensities of the C−H stretching vibrations at 2945 cm^{-1} as well as an ester peak at 1765 cm^{-1}. Most of the PLGA inclusions were seen in the periphery of the nucleus at 2 h, much earlier than the aggregations of the PCL particles. Similar to the PCL system, the carriers did not seem to follow any specific subcellular targeting patterns but were rather distributed throughout the cell body. The proximity of the aggregating nanoparticles in the perinuclear region depicts the possible integration of PLGA with intracellular structures such as the ER and Golgi. This has been also observed utilizing opossum kidney (OK) renal tubule and human bronchial epithelial (HBE) cell lines.[18]

Incubation of the cell cultures with fresh medium following the PLGA-nanoparticle-containing medium showed degradation of the nanoparticle system, as shown in Figure 5. After 3 h of incubation in fresh medium, the PLGA signal was not detected as a separate endmember; however, smaller lipid or phospholipid inclusions were still distributed throughout the cell body (Figure 5, middle row). The inclusions, however, did have a preference for the perinuclear regions, co-localizing with the ER and the Golgi apparatus. The

two membrane-rich cytoplasmic structures are shown in green in the images. The C−H stretching region of the green endmember has features attributed to high phospholipid content—prevalent in vesicle formations—overlaid with the signatures coming from diverse perinuclear organelles, which resulted in the broadening of the peak. This is further seen from the peak attributed to the ester linkages at 1765 cm^{-1}, which disappears after 3−6 h incubation in fresh medium. This is followed by an increase of the band at 1740 cm^{-1}, characteristic of diverse lipid and phospholipid formations. This is consistent with the previous studies of PLGA nanoparticles being sorted into Golgi-associated late endosomes.[18,38] These inclusions completely disappear after 6 h of incubation in fresh medium, as indicated by only two spectral endmembers, one for nucleus and cell body (blue) and another for ER- and Golgi-rich regions (green). This shows a complete digestion of the introduced PLGA nanoparticles.

Cellular degradations of PLGA beads (phagocytosed by macrophages) have been analyzed earlier using Raman imaging[45] by following the ester linkage band. The particles investigated, however, were significantly larger, on the order of 10 μm in size. The findings illustrated a long-term (1−2 weeks), cell-mediated degradation process, which underscored a homogeneous degradation of microspheres,[45,46] via the hydrolysis of the ester linkages in parallel with enzymatic degradation. Since HeLa cells

are nonphagocytic, the nanoparticulate internalization yielded intracellular aggregates in sizes no larger than 1−2 μm, and hence, the interparticle degradations were not observed. The degradation kinetics were also faster due to the nanometer size of the introduced nanocarriers.

Our results closely parallel previous studies showing PCL degradation patterns much slower than those of PLGA, remaining intact particles in the cell body.[4,18,32,47] The exact intracellular pathway of the nanoparticles is still not fully known. However, it has been suggested that nanoparticle degradation may follow a number of pathways such as mere entrapment in the sorting vesicles, excretion from recycling endocytotic vesicles, or lysosome degradation.[38] As the particles are incorporated into the cell body, their chemical signatures are easily distinguished from the rest of the cell; however, as the catabolic pathways proceed, shifting, decreasing/increasing peak heights, and ratios in the rendered Raman spectra delineate the system's degradation paths.

The noninvasive character of Raman imaging as well as the associated chemical information has previously been used for in vivo studies of mice, evaluating the tumor-targeting ability of carbon nanotubes.[13,21] Raman imaging can thus monitor the path of nanoparticles via their characteristic frequencies of vibrational bands without the use of external labels. Their distinct intracellular kinetics and dynamics can be assessed, revealing specificity (if any) of the nanovehicle to a target organelle. Upon the penetration of the particle inside the cell and its further recognition of the organelle, the biochemical interactions can be extrapolated from the spectra. With this technique, we can noninvasively monitor the incorporation and subsequent specificity of the carrier system.

METHODS

Cell Culture. Human HeLa cells (cell line CCL-2, ATCC, Manassas, VA) were grown in 75 cm^3 culture flasks (Fisher Scientific) with 7 mL of Dulbecco's Modified Eagle's medium (DMEM, ATCC) and 10% fetal bovine serum (FBS, ATCC). Cells were incubated at 37 °C and 5% CO_2. Cells were grown on CaF_2 windows to avoid scattering from the regular glass windows. Prior to data collection, cells were fixed in a 10% phosphate-buffered formalin solution (Sigma-Aldrich, St. Louis, MO) and washed in phosphate-buffered saline.

Incubations with PCL and PLGA nanoparticles were carried out at 37 °C. All Raman measurements were performed at room temperature.

PCL or PLGA Nanoparticle Preparation. PCL/Pluronic F-108 and PLGA/Pluronic F-108 blend nanoparticles were prepared using solvent displacement in an acetone/water system as previously described.[48] In short, a solution of PCL or PLGA was prepared in acetone or ethanol, respectively, and was introduced into an aqueous solution containing known concentrations of Pluronic (F-68 or F-108) under magnetic stirring. Typically, a 1% (w/v) solution of PCL in 50 mL of acetone was introduced into an aqueous solution of Pluronic. The rate of addition was controlled through a buret at about 1 mL/min, and stirring was maintained at a speed that facilitated formation of a vortex in the solution. The nanoparticles were freeze-dried as such (with surfactant remaining in the bulk) or after removal of excess (unadsorbed) stabilizer either by centrifugation (10 000 rpm for 20 min followed by washing twice with 50 mL of water) and/or equilibrium dialysis (against water using dialysis membrane having 15 000 Da cutoff—from Spectrum Laboratories, USA, which results in selective leaching of free Pluronics in solution through the membrane).

Raman Data Acquisition. The cellular images presented in this paper were recorded using a CRM200 confocal Raman microscope (WITec GmbH, Ulm, Germany) employing 488 nm (ca. 30 mW at 488 nm) excitation wavelength and a water immersion objective (60×/NA = 1.00, WD = 2.0 mm), with resolution or step size of 500 nm and 250 ms exposure time. Excitation is provided by an air-cooled Ar ion laser (Melles Griot, model 532). The exciting laser radiation is coupled into a Zeiss microscope through a wavelength-specific single-mode optical fiber. The incident laser beam is collimated via an achromatic lens and passes a holographic band-pass filter before it is focused onto the sample through the microscope objective.

The sample is located on a piezo-electrically driven microscope scanning stage with an x,y resolution of ca. 3 nm and a repeatability of ±5 nm and z resolution of ca. 0.3 nm and ±2 nm repeatability. The sample is scanned through the laser focus in a raster pattern at a constant stage speed of fractions of a micrometer per second. The continuous motion prevents sample degradation at the focal point of the laser beam. Spectra are collected at a 0.5 μm grid, with a dwell time of 0.5 s.

Raman backscattered radiation was collected through the microscope objective and passed through a holographic edge filter to block Rayleigh scattering and reflected laser light before being focused into a multimode optical fiber. The 50 μm diameter single-mode input fiber and the 50 μm diameter multimode output fiber provided the optical apertures for the confocal measurement. The light emerging from the output optical fiber was dispersed by a 30 cm focal length, f/4 Czerny−Turner monochromator, incorporating interchangeable gratings (1800/mm, blazed at 500 nm, and 600/mm, blazed at 500 nm). The light was finally detected by a back-illuminated deep-depletion, 1024 × 128 pixel charge-coupled device camera operating at −82 °C.

REFERENCES AND NOTES

1. Csaba, N.; Garcia-Fuentes, M.; Alonso, M. Nanoparticles for Nasal Vaccination. *Adv. Drug Delivery Rev.* **2009**, *61*, 140–157.
2. Lai, S.; Wang, Y.-Y.; Hanes, J. Mucus-Penetrating Nanoparticles for Drug and Gene Delivery to Mucosal Tissues. *Adv. Drug Delivery Rev.* **2009**, *61*, 158–171.
3. Kaul, G.; Amiji, M. Tumor-Targeted Gene Delivery Using Poly(ethylene glycol)-Modified Gelatin Nanoparticles: *In Vitro* and *In Vivo* Studies. *Pharm. Res.* **2005**, *22*, 951–961.
4. Chawla, J.; Amiji, M. Biodegradable Poly(ε-caprolactone) Nanoparticles for Tumor-Targeted Delivery of Tamoxifen. *Int. J. Pharm.* **2002**, *249*, 127–138.
5. Kaul, G.; Amiji, M. Long-Circulating Poly(ethylene glycol)-Modified Gelatin Nanoparticles for Intracellular Delivery. *Pharm. Res.* **2002**, *19*, 1061–1067.
6. Uhrich, K.; Cannizzaro, S.; Langer, R.; Shakesheff, K. Polymeric Systems for Controlled Drug Release. *Chem. Rev.* **1999**, *99*, 3181–3198.
7. Torchilin, V. Recent Approaches to Intracellular Delivery of Drugs and DNA and Organelle Targeting. *Annu. Rev. Biomed. Eng.* **2006**, *8*, 343–375.

8. Torchilin, V. Multifunctional Nanocarriers. *Adv. Drug Delivery Rev.* **2006**, *58*, 1532–1555.

9. Hinman, L.; Hamann, P.; Wallace, R.; Menendez, A.; Durr, F.; Upeslacis, J. Preparation and Characterization of Monoclonal Antibody Conjugates of the Calicheamicins: A Novel and Potent Family of Antitumor Antibiotics. *Cancer Res.* **1993**, *53*, 3336–3342.

10. Rao, J. Shedding Light on Tumors Using Nanoparticles. *ACS Nano* **2008**, *2*, 1984–1986.

11. Torchilin, V. *Nanoparticulates as Drug Carriers*; Imperial College Press: London, UK, 2006.

12. Brown, R.; Links, M. Clinical Relevance of the Molecular Mechanisms of Resistance to Anti-Cancer Drugs. *Expert Rev. Mol. Med.* **1999**, *1*, 1–21.

13. Zavaleta, C.; de la Zerda, A.; Liu, Z.; Keren, S.; Cheng, Z.; Schipper, M.; Chen, X.; Dai, H.; Gambhir, S. Noninvasive Raman Spectroscopy in Living Mice for Evaluation of Tumor Targeting with Carbon Nanotubes. *Nano Lett.* **2008**, *8*, 2800–2805.

14. Smith, B.; Cheng, Z.; De, A.; Koh, A.; Sinclair, R.; Gambhir, S. Real-Time Intravital Imaging of RGD-Quantum Dot Binding to Luminal Endothelium in Mouse Tumor Neovasculature. *Nano Lett.* **2008**, *8*, 2599–2606.

15. Cai, W.; Shin, D.-W.; Chen, K.; Gheysens, O.; Cao, Q.; Wang, S. X.; Gambhir, S. S.; Chen, X. Peptide-Labeled Near-Infrared Quantum Dots for Imaging Tumor Vasculature in Living Subjects. *Nano Lett.* **2006**, *6*, 669–676.

16. Tang, N.; Du, G.; Wang, N.; Liu, C.; Hang, H.; Liang, W. Improving Penetration in Tumors with Nanoassemblies of Phospholipids and Doxorubicin. *J. Natl. Cancer Inst.* **2007**, *99*, 1004–1015.

17. Stroh, M.; Zimmer, J.; Duda, D.; Levchenko, T.; Cohen, K.; Brown, E.; Scadden, D.; Torchilin, V.; Bawendi, M.; Fukumura, D.; Jain, R. Quantum Dots Spectrally Distinguish Multiple Species within the Tumor Milieu *In Vivo*. *Nat. Med.* **2005**, *11*, 678–682.

18. Cartiera, M.; Johnson, K.; Rajendran, V.; Caplan, M.; Saltzman, W. The Uptake and Intracellular Fate of PLGA Nanoparticles in Epithelial Cells. *Biomaterials* **2009**, *30*, 2790–2798.

19. Nijssen, A.; Koljenović, S.; Bakker Schut, T.; Caspers, P.; Puppels, G. Towards Oncological Application of Raman Spectroscopy. *J. Biophoton.* **2009**, *2*, 29–36.

20. Ellis, D.; Goodacre, R. Metabolic Fingerprinting in Disease Diagnosis: Biomedical Applications of Infrared and Raman Spectroscopy. *Analyst* **2006**, *131*, 875–885.

21. Keren, S.; Zavaleta, C.; Cheng, Z.; de la Zerda, A.; Gheysens, O.; Gambhir, S. Noninvasive Molecular Imaging of Small Living Subjects Using Raman Spectroscopy. *Proc. Natl. Acad. Sci. U.S.A.* **2008**, *105*, 5844–5849.

22. Uzunbajakava, N.; Lenferink, A.; Kraan, Y.; Volokhina, E.; Vrensen, G.; Greve, J.; Otto, C. Nonresonant Confocal Raman Imaging of DNA and Protein Distribution in Apoptotic Cells. *Biophys. J.* **2003**, *84*, 3968–3981.

23. van Manen, H.-J.; Kraan, Y.; Roos, D.; Otto, C. Single-Cell Raman and Fluorescence Microscopy Reveal the Association of Lipid Bodies with Phagosomes in Leukocytes. *Proc. Natl. Acad. Sci. U.S.A.* **2005**, *102*, 10159–10164.

24. Matthäus, C.; Kale, A.; Chernenko, T.; Torchilin, V.; Diem, M. New Ways of Imaging Uptake and Intracellular Fate of Liposomal Drug Carrier Systems Inside Individual Cells, Based on Raman Microscopy. *Mol. Pharmaceutics* **2008**, *5*, 287–293.

25. Matthäus, C.; Chernenko, T.; Newmark, J.; Warner, C.; Diem, M. Label-Free Detection of Mitochondrial Distribution in Cells by Nonresonant Raman Microspectroscopy. *Biophys. J.* **2007**, *93*, 668–673.

26. Matthäus, C.; Boydston-White, S.; Miljković, M.; Romeo, M.; Diem, M. Raman and Infrared Microspectral Imaging of Mitotic Cells. *Appl. Spectrosc.* **2006**, *60*, 1–8.

27. Krafft, C.; Knetschke, T.; Funk, R.; Salzer, R. Studies on Stress-Induced Changes at the Subcellular Level by Raman Microspectroscopic Mapping. *Anal. Chem.* **2006**, *78*, 4424–4429.

28. Otto, C.; Sijtsema, N.; Greve, J. Confocal Raman Microspectroscopy of the Activation of Single Neutrophilic Granulocytes. *Eur. Biophys. J* **1998**, *27*, 582–589.

29. Matthäus, C.; Chernenko, T.; Quintero, L.; Milane, L.; Kale, A.; Amiji, M.; Torchilin, V.; Diem, M. Raman Microscopic Imaging of Cells and Applications Monitoring the Uptake of Drug Delivery Systems. *SPIE* **2008**, *6991*, 699106.

30. Diem, M.; Matthäus, C.; Chernenko, T.; Romeo, M.; Miljković, M.; Bird, B.; Schubert, J.; Papamarkakis, K.; Bedrossian, K.; Laver, N. Infrared and Raman Spectroscopy and Spectral Imaging of Individual Cells. In *Infrared and Raman Spectroscopic Imaging*; Salzer, R., Siesler, H. W., Eds.; Wiley-VCH: Weinheim, Germany, 2009; Vol. 17, pp 3−202.

31. Movasaghi, Z.; Rehman, S.; Rehman, I. Raman Spectroscopy of Biological Tissues. *Appl. Spectrosc. Rev.* **2007**, *42*, 493–541.

32. Pitt, C. Poly-ε-caprolactone and Its Copolymers. In *Biodegradable Polymers as Drug Delivery Systems*; Langer, R., Chasin, M., Eds.; Marcel Decker Inc: New York, 1990; pp 71−120.

33. Maeda, H.; Wu, J.; Sawa, T.; Matsumura, Y.; Hori, K. Tumor Vascular Permeability and the EPR Effect in Macromolecular Therapeutics: A Review. *J. Controlled Release* **2000**, *65*, 271–284.

34. Sivalingam, G.; Chattopadhyay, S.; Madras, G. Enzymatic Degradation of Poly(ε-caprolactone), Poly(vinyl acetate) and Their Blends by Lipases. *Chem. Eng. Sci.* **2003**, *58*, 2911–2919.

35. Gan, Z.; Yu, D.; Zhong, Z.; Liang, Q.; Jing, X. Enzymatic Degradation of Poly(ε-caprolactone)/Poly(-lactide) Blends in Phosphate Buffer Solution. *Polymer* **1999**, *40*, 2859–2862.

36. Matthäus, C.; Chernenko, T.; Quintero L.; Miljković, M.; Milane, L.; Kale A.; Amiji M.; Torchilin V.; Diem M. Raman Micro-spectral Imaging of Cells, and Applications Monitoring the Uptake of Drug Delivery Systems. In *Confocal Raman Imaging*; Dieing, T., Toporski, J., Hollricher, O., Eds.; Springer Verlag: Heidelberg, Germany, in press.

37. Nascimento, J.; Dias, J. Vertex Component Analysis: A Fast Algorithm to Unmix Hyperspectral Data. *IEEE Trans. Geosci. Remote Sens.* **2005**, *43*, 898–910.

38. Panyam, J.; Labhasetwar, V. Targeting Intracellular Targets. *Curr. Drug Delivery* **2004**, *1*, 235–247.

39. Krafft, C.; Neudert, L.; Simat, T.; Salzer, R. Near Infrared Raman Spectra of Human Brain Lipids. *Spectrochim. Acta, Part A* **2005**, *61*, 1529–1535.

40. Matthäus, C.; Chernenko, T. In *Vibrational Spectroscopy for Medical Diagnosis*; Diem, M., Griffiths, J., Chalmers, J., Eds.; John Wiley & Sons: New York, 2008; pp 325−333.

41. Panyam, J.; Labhasetwar, V. Biodegradable Nanoparticles for Drug and Gene Delivery to Cells and Tissue. *Adv. Drug Delivery Rev.* **2003**, *55*, 329–347.

42. Panyam, J.; Labhasetwar, V. Dynamics of Endocytosis and Exocytosis of Poly(D,L-Lactide-*co*-Glycolide) Nanoparticles in Vascular Smooth Muscle Cells. *Pharm. Res.* **2003**, *20*, 212–220.

43. Rosenberg, R.; Devenney, W.; Siegel, S.; Dan, N. Anomalous Release of Hydrophilic Drugs from Poly(ε-caprolactone) Matrices. *Mol. Pharmaceutics* **2007**, *4*, 943–948.

44. Weng, K.; Noble, C.; Papahadjopoulos-Sternberg, B.; Chen, F.; Drummond, D.; Kirpotin, D.; Wang, D.; Hom, Y.; Hann, B.; Park, J. Targeted Tumor Cell Internalization and Imaging of Multifunctional Quantum Dot-Conjugated Immunoliposomes *In Vitro* and *In Vivo*. *Nano Lett.* **2008**, *8*, 2851–2857.

45. van Apeldoorn, A.; van Manen, H.; Bezemer, J.; de Bruijn, J.; van Blitterswijk, C.; Otto, C. Raman Imaging of PLGA Microsphere Degradation Inside Macrophages. *J. Am. Chem. Soc.* **2004**, *126*, 13226–13227.

46. Li, S. Hydrolytic Degradation Characteristics of Aliphatic Polyesters Derived from Lactic and Glycolic Acids. *J. Biomed. Mater. Res.* **1999**, *48*, 342–353.

47. Sung, H.-J.; Meredith, C.; Johnson, C.; Galis, Z. The Effect of Scaffold Degradation Rate on Three-Dimensional Cell Growth and Angiogenesis. *Biomaterials* **2004**, *25*, 5735–5742.

48. Shenoy, D.; Amiji, M. Poly(ethylene oxide)-Modified Poly(ε-caprolactone) Nanoparticles for Targeted Delivery of Tamoxifen in Breast Cancer. *Int. J. Pharm.* **2005**, *293*, 261–270.